Available online at https://link.springer.com/journal/42241
http://www.jhydrodynamics.com
Journal of Hydrodynamics, 2020, 32(1): 20-30
https://doi.org/10.1007/s42241-020-0003-7

Numerical investigation on free surface effect on the supercavitating flow over a low aspect ratio wedge-shaped hydrofoil *

Chang Xu, Boo Cheong Khoo
Department of Mechanical Engineering, National University of Singapore, Singapore

(Received December 26, 2019, Revised January14, 2020, Accepted January 15, 2020, Published online March 4, 2020)

Abstract: In this study, the effect of the free surface on the supercavitating flow that surrounds a low aspect ratio wedge-shaped hydrofoil is studied based on computational fluid dynamics (CFD), with Cartesian cut-cell mesh method. The volume of fraction (VOF) method and the k-ε turbulence model with the Schnerr Sauer cavitation model are used for simulating the supercavitation in turbulent flow. Both quasi-3-D and full-3-D cases are considered. The quasi-3-D simulation results are compared with the previous water tunnel experimental data and analytical data, and the results agree well with each other. The results are presented for a wide range of submerged distance in terms of the free surface effect on the cavity shape, wave elevation and force coefficients. The range of the free surface effect is found. The simulation results show that the cavitating flow around the hydrofoil become shorter and thicker as the submerge depth decreases. As the aspect ratio of the hydrofoil studied in the full-3-D cases is low, the 3-D effect on the supercavitating flow is strong. The relationship between the flow patterns and vortex structures is also revealed from the numerical results.

Key words: Supercavitating flow, hydrofoil, multiphase flow, free surface effect

Introduction

The study on the supercavitating flow started in the early 20th century owing to the development of increasing high-speed underwater vehicles and surface piercing hydrofoil craft. When a vehicle moves fast underwater, liquid water is subjected to rapid pressure changes that cause the formation of cavities in a low-pressure region[1-2]. For a typical high-speed hydrofoil craft, the process can be considered/interpreted as a representative problem of the unsteady transient cavitating flow and its interaction with the nearby free surface[3-7]. The influence of cavitating flow on the performance of high speed navigation vehicle cannot be neglected.

The issues have been studied by several researchers using different experimental and numerical approaches[8-10]. Mostly, the relevant experiments are performed in water tunnel[11], towing tank or free launching test system[12]. The measurement instruments such as high-speed video camera system, particle image velocimetry[13-14] and X-ray imaging[15] are widely used in the experiments to observe the flow motion and cavity structures. Besides, the CFD methods are also increasingly used for simulating the cavitating flow by solving the incompressible Navier-Stokes equations with various cavitation and turbulence models, among which the modified renormalization-group k-ε turbulence model[16-18], the filter-based k-ε model[19], and the partially-averaged Navier-Stokes method[20-21], are widely used.

However, most previous works on supercavitating flow have focused largely on the fully submerged conditions. There are essentially two main types of supercavitating flow: natural cavitation and artificial ventilation[22-25], which are considered as an important and widely used control approach in the cavitating flow for drag reduction[26]. During the cruise, the medium in contact with the underwater vehicle changes from water to vapor. Since the vapor density is much less than the water, the resistance of the vehicle can therefore be greatly reduced. The complex unsteadiness of the resulting supercavitating flow has been studied in recent years[27-28].

In this paper, we have extended the study from fully submerged cases to near free surface cases, which may invariably affect the cavity shape, cavity evolution process and force coefficients. Figure 1 shows a schematic of the supercavitating flow around

* **Biography:** Chang Xu (1983-), Female, Ph. D.,
E-mail: e0348786@u.nus.edu
Corresponding author: Boo Cheong Khoo,
E-mail: mpekbc@nus.edu.sg

the wedge-shaped hydrofoil placed near the free surface. The reference point O and the parameters include the submerged depth of the hydrofoil (s), the cord length (c), the trailing edge thickness (t), the angle of attack (α), the free stream velocity (U_∞), the cavity length (l), and the maximum cavity thickness (δ) are indicated in the figure. The supercavitating flow is investigated in this paper using the CFD simulation, with a focus on the effect of free surface near the hydrofoil. The numerical methods are validated against previous experimental results[29] and analytical data[7, 19] for the quasi-3-D cases. The cavitating evolution process on a typical working condition is discussed first to show the flow patterns. The supercavitating flow on the upper and lower sides of the hydrofoil are found to fuse after a certain time and then continues to grow backwards to the final stable state. The submerged depth of the hydrofoil is varied to analyze the free surface effect on the cavity shape, wave elevation, force coefficients and the range of the free surface effect. Finally, full-3-D simulations are also conducted to investigate the 3-D effect of the supercavitating flow in the vicinity of the free surface.

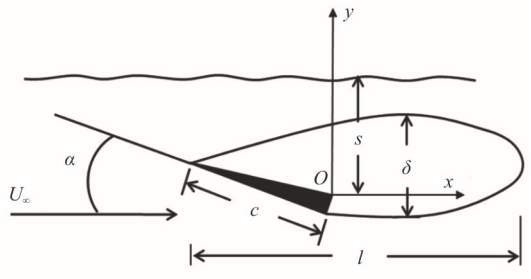

Fig. 1 Schematic of the supercavitating flow around the wedge-shaped hydrofoil near free surface

1. Numerical methods

1.1 *Governing equations*

The multiphase flow equations are extensively used for solving the multiphase flow problems. The continuity and momentum equations are expressed as:

$$\frac{\partial \rho}{\partial t}+\frac{\partial \rho}{\partial x_j}=0 \tag{1}$$

$$\frac{\partial(\rho u_i)}{\partial t}+\frac{\partial(\rho u_i u_j)}{\partial x_j}=-\frac{\partial p}{\partial x_j}+\frac{\partial}{\partial x_j}\left(\mu\frac{\partial u_j}{\partial x_j}\right) \tag{2}$$

where u_i is the velocity component in the i-direction, ρ is the mixture density, p is the pressure and μ is the laminar flow viscosity, which can be defined as

$$\mu=(1-\alpha_v-\alpha_a)\mu_l+\alpha_v\mu_v+\alpha_a\mu_a \tag{3}$$

where α is the volume fraction of the different phases. The subscripts a, l and v represent the air, liquid water and water vapor, respectively. The density ρ of the mixture is defined as

$$\rho=(1-\alpha_v-\alpha_a)\rho_l+\alpha_v\rho_v+\alpha_a\rho_a \tag{4}$$

where the subscripts are defined the same. The transport equations of the air and water vapor volume fraction are

$$\frac{\partial(\alpha_a\rho_a)}{\partial t}+\frac{\partial(\alpha_a\rho_a u_j)}{\partial x_j}=0 \tag{5}$$

$$\frac{\partial(\alpha_v\rho_v)}{\partial t}+\frac{\partial(\alpha_v\rho_v u_j)}{\partial x_j}\doteq\dot{m} \tag{6}$$

where $\dot{m}$ is the mass transfer rate which is modeled by mass transfer cavitation model. In this case, the Schnerr Sauer mass transfer model is used

$$\dot{m}=-3\rho v^3\sqrt{n_0\frac{4}{3}\pi\left[\alpha^2-\alpha^3\left(1-\frac{\rho_v}{\rho_l}\right)\right]}\operatorname{sign}(p_v-p)\cdot\sqrt{\frac{2}{3}\frac{|p_v-p|}{\rho_l}} \tag{7}$$

In this model, the number of vapor bubbles per volume of liquid (n_0) is set to a value of 1.5×10^{14} nuclei/$\mathrm{m}^3_{\mathrm{water}}$. This setting have been discussed in Ref. [30] and found to work well for a variety of fluids and devices.

The standard k-ε turbulence model with the transport equations for the turbulent kinetic energy k and its dissipation rate ε was adopted for turbulent flow closure. The turbulent flow viscosity is given as $\mu_t=\rho C_\mu k^2/\varepsilon$. The turbulence kinetic energy and its rate of dissipation are obtained from the transport equations:

$$\frac{\partial}{\partial t}(\rho_m k)+\nabla\cdot(\rho_m \boldsymbol{k}\boldsymbol{v}_m)=\nabla\cdot\left[\left(\mu+\frac{\mu_t}{\sigma_t}\right)\nabla k\right]+G_k-\frac{2}{3}\rho(\nabla\cdot u)k-\rho\varepsilon+S_k \tag{8}$$

$$\frac{\partial}{\partial t}(\rho_m\varepsilon)+\nabla\cdot(\rho_m\varepsilon\boldsymbol{v}_m)=\nabla\cdot\left[\left(\mu+\frac{\mu_t}{\sigma_\varepsilon}\right)\nabla\varepsilon\right]+$$

$$C_{1\varepsilon}G_k\frac{\varepsilon}{k}-\left(\frac{2}{3}C_{1\varepsilon}-C_{3\varepsilon}\right)\rho(\nabla\cdot u)\varepsilon-C_{2\varepsilon}\rho\frac{\varepsilon^2}{k}+S_\varepsilon \tag{9}$$

where C_μ is an empirical constant of 0.09. The model constants $C_{1\varepsilon}$, $C_{2\varepsilon}$, $C_{3\varepsilon}$, σ_t and σ_ε are 1.44, 1.92, 0, 1.0 and 1.3, respectively.

1.2 *Numerical schemes and parameters*

A 114.45 mm long, 80.26 mm wide and 12.27 mm high wedge-shaped hydrofoil model is studied here (shown in Fig. 2). The distance between the wedge-shaped hydrofoil and the free surface over the chord length (s/c) varies from 0.8300 to 2.1600 and the simulated cavitation number varies from 0.1 to 0.2 at different angle of attack (8°, 10°, 12°), which are kept the same as those in the water tunnel experiment[29]. In this work, both quasi-3-D and full-3-D flow simulations are carried out to study the supercavitating flow around the hydrofoil. For the quasi-3-D cases, the computational domain is a 1500.00 mm long×80.26 mm wide×100.00 m high with the boundary conditions defined at the velocity-inlet, the pressure-outlet, and no-slip wall as shown in Fig. 3. Other simulation conditions are consistent with the water tunnel experiment. The cavitation number can be calculated using the following formula

$$\sigma=\frac{p_\infty-p_v}{0.5\rho U_\infty{}^2} \tag{10}$$

where $p_\infty=101.325$ kPa is the standard atmospheric pressure, $p_v=2\,450$ Pa is the saturated vapor pressure, $\rho=1\,000$ kg/m^3 is the liquid water density and U_∞ is the free stream velocity.

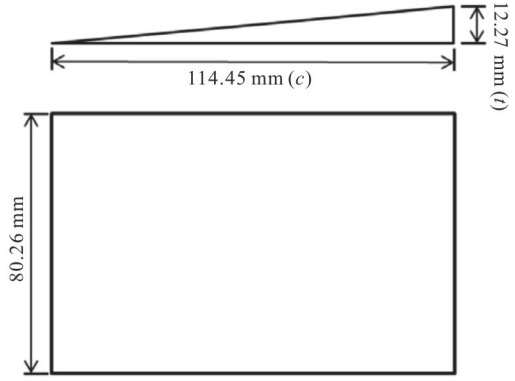

Fig. 2 Wedge model in water tunnel experiment (side view/ plan view)

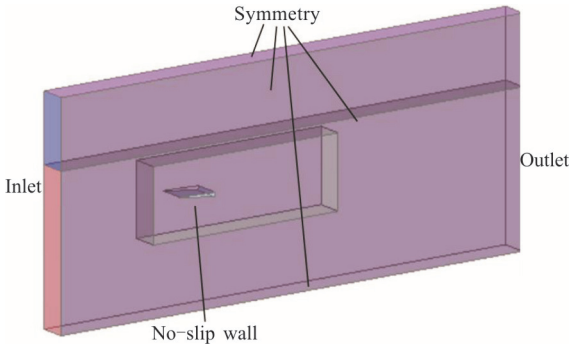

Fig. 3 (Color online) Schematic of the computational domain and boundary conditions of the quasi-3-D cases

The Cartesian cut-cell mesh method is used to generate an unstructured mesh with 15 layers of inflation. The minimum face size of the hydrofoil model is 1×10^{-3} m. The height of the first layer is set to 5×10^{-5} m with a growth rate of 1.1 in the mesh plan to ensure that y^+ is approximately equal to 1, and a higher mesh resolution around the wedge-shaped hydrofoil and downstream in its wake so as to be able to capture the interface between the liquid water and vapor phases accurately. Figure 4 shows that the spatial volume grids are composed of cubes of different sizes. The total cell number is approximately 2×10^6 with good orthogonality.

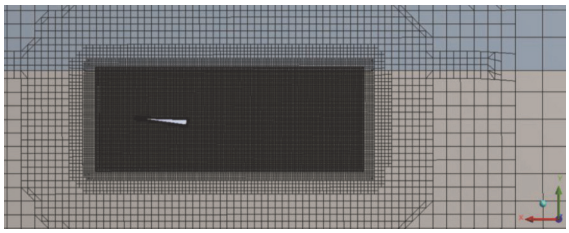

Fig. 4 (Color online) Mesh layout of the flow field surrounding the hydrofoil

Separately, to consider the 3-D effect of the supercavitating flow, another five full-3-D simulations have been performed. The simulations are carried out in a 1 500.00 mm long×400.00 mm wide×100.00 mm high computational domain with the defined boundary conditions are shown in Fig. 5 to consider the full-3-D effect. Here the distance between the boundaries perpendicular to the spanwise direction and the hydrofoil is about two times chord length to avoid the interactions between the boundaries and the supercavitating flow. The Cartesian cut-cell mesh method with the same characteristics of the quasi-3-D mesh plan is used here. The total cell size is about 8×10^6 with good orthogonality.

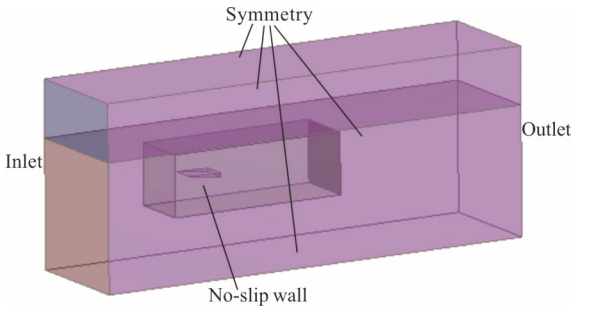

Fig. 5 (Color online) Schematic of the computational domain and boundary conditions of the full-3-D cases

1.3 *Validation*

Literature focusing on the supercavitating flow around hydrofoil under the free surface effect is limited. It is difficult to produce a stable free surface in a cavitation water tunnel and to obtain credible experimental results. Several early but successful experiments were carried out by Dawson[29] who studied the supercavitating flow around a wedge-shaped hydrofoil near the free surface. In his study, various submerged depth, cavitation number and angle of attack of the hydrofoil are considered. The hydrofoil model is mounted on a spindle disk attached to the cavitation tunnel walls. Due to the low-velocity restriction in the cavitation tunnel, the supercavitating flow in the experiments was generated by ventilation. In the preliminaries, both theoretical approaches and numerical methods are employed to compare and analyze the supercavitating flow in the experiment. Wu[31] conducted a wake model for the free-streamline theory, which can be applied to the 2-D flow past an inclined flat plate with a wake or cavity formation. Faltinsen and Semenov[7] had studied the characteristics of the supercavitating flow around a flat plate by analytical means and is utilized here for comparison. The influences of the free surface and gravity on the cavity profile, free surface elevation and force coefficient are discussed.

For validation, our simulated results are compared with Dawson's experimental data, the analytical solution of Faltinsen and Semenov, Wu's theory for a weightless infinite fluid medium. More specifically, we compared the normal force coefficient (c_n) versus cavitation number (σ), at three angles of attack (8°, 10°, 12°) and submerged depth over cord length (s/c) equals to 0.8300 as shown in Fig. 6. It may be noted that Wu had established a wake model for the supercavitating flow past an oblique flat plate without considering the influence of free surface effect. The comparison in Fig. 6 for c_n versus σ at various angle of attack is fair: the much closer agreement between the simulation and experiment (considering the experimental uncertainty of measurements in the experiment estimated to be 1.2% to 3.2%) clearly attested to the validity of the numerical model with the back drop of the analytical approach[7, 31] (considering the limitations of the assumptions associated) providing the trend in broad agreement. Here, the component of the normal force F_n is normal to the hydrofoil and c_n is defined as

$$c_n = \frac{F_n}{\rho U_\infty^2 c/2} \tag{11}$$

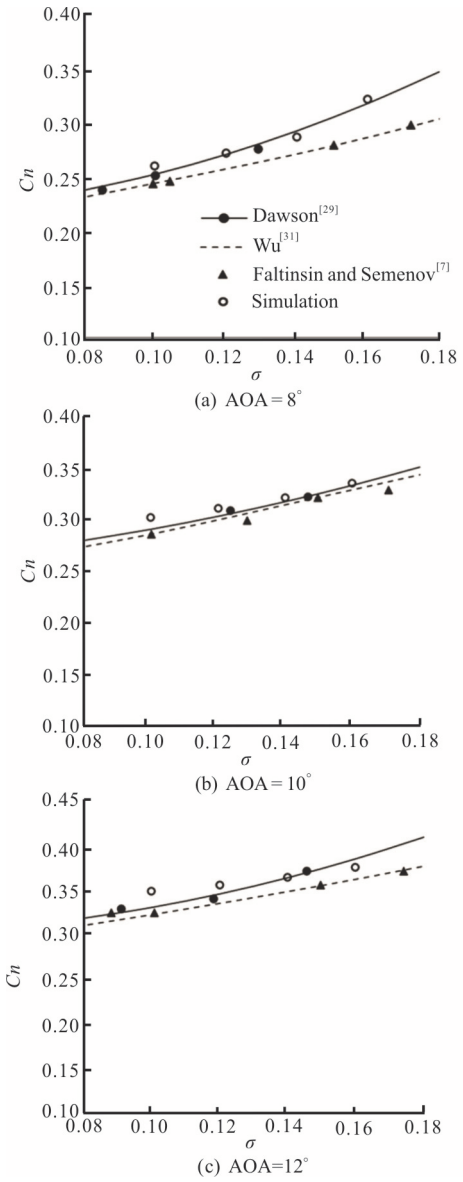

Fig. 6 Comparison of the experimental data and the numerical results of the normal force coefficient versus cavitation number at $s/c = 0.8300$, AOA = 8°, 10° and 12°

Further detailed comparison of the pressure distribution on the upper surface of the wedge-shaped hydrofoil at $s/c = 0.8300$, AOA = 8°, $\sigma = 0.128$

between the experiment and simulation is given in Fig. 7. Here the pressure coefficient c_p is defined as

$$c_p = \frac{p - p_v}{\rho U_\infty{}^2 / 2} \tag{12}$$

Dawson mentioned that the pressure measurements by water monometer in the experiment are considered accurate to within 0.01 feet of water, which is equivalent to about 1.2% to 3.2%. Considering the measurement uncertainty, the comparison in Fig. 7 further attests to the validity of our numerical simulation besides the earlier comparison in Fig. 6 based on the integrated force quantity.

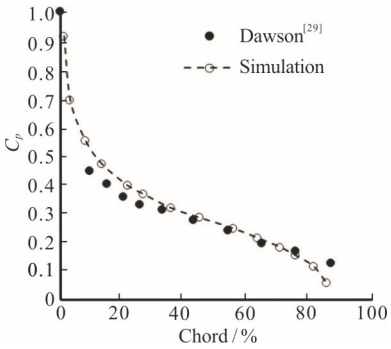

Fig. 7 Comparison of the experimental and numerical results of the pressure distribution on the upper surface of the wedge-shaped hydrofoil at $s/c = 0.8300$, AOA $= 8°$ and $\sigma = 0.128$

2. Results and discussion

2.1 *Cavity evolution process*

In order to study the characteristics of the supercavitating flow under the free surface effect, we first need to understand the evolution mechanism in the growth of the supercavity. Figure 8 shows the dimensionless cavity length (l/c) growth with dimensionless time $(\tau = tU_\infty / c)$ for the simulated cases at the angle of attack of 8° and cavitation number of 0.1 under the free surface effect. The submerged depth over cord length (s/c) of the hydrofoil at 0.8300, 1.1625, 1.495, 1.8275 and 2.1600 are considered. In the nominally-termed first stage, the cavity growth rate under the different conditions is almost the same for $\tau \le 1.5$. At $\tau \cong 1.5$, the cavity on the upper and back sides of the hydrofoil fuses, and the evolution of the cavity enters the second stage. The growth rate of the cavitating flow then becomes less intense compared to the first stage. Cavitating flow still continues to grow backwards after fusion. In the third stage, the growth rate of the cavity decreased sharply after $\tau \cong 9.2$, and the cavity profile was basically stable. For different submerged depths, the growth rate and length of the cavity decrease as the hydrofoil moves closer to the free surface. The range of the free surface effect on the supercavitating flow is also limited: from the results, the gradient of the cavity length growth for $s/c = 1.8275$, 2.1600 are basically coincident. In another word, beyond say $s/c \cong 2.0000$, the effect of free surface is largely non-existent or only very minimal akin to infinite medium without the presence of free surface.

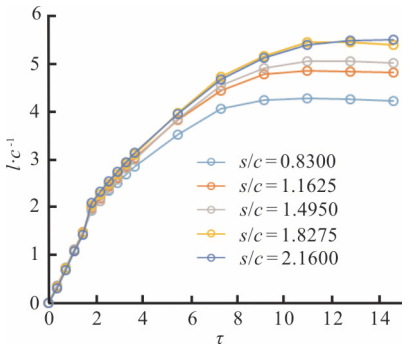

Fig. 8 (Color online) Dimensionless cavity length grow with dimensionless time for the simulated cases at AOA $= 8°$, $\sigma = 0.100$ under the free surface effect. The submerged depth over cord length of the hydrofoil $s/c = 0.8300$, 1.1625, 1.4950, 1.8275 and 2.1600

In general, the cavity evolution process of the supercavitating flow over the wedge-shaped hydrofoil in this study mainly contains three stages as discussed. Next, we choose a typical working condition to analyze more closely the characteristics of the cavity profile during the evolution process in the first stage. Figure 9 shows the simulated results at AOA $= 8°$, $\sigma = 0.100$, submerged depth over cord length s/c of the hydrofoil at 0.8300 under the influence of free surface effect. At $\tau = 0.4$, cavity starts appearing on the upper and trailing edge of the hydrofoil and grows backward with time for both the upper and trailing edge surfaces. It can be seen that the two parts of the cavity meet and fuse at around $\tau \cong 1.5$. At $\tau = 2.2$, the fusion process of the cavitation ends, and the supercavitating flow continues to flow backward to the final stable state.

The vortex structure of the cavitating flow around the hydrofoil during the cavity growth stage is also shown Fig. 10. The flow structures can be visualized based on the Q - criterion[32]. It clearly shows that the motion of cavitation clouds has strong correlation with the vortex motion.

2.2 *On the interaction between free surface and supercavitating flow*

The problem with the supercavitating flow near the free surface generally consists of two parts, the free surface effect on the supercavity and the effect of

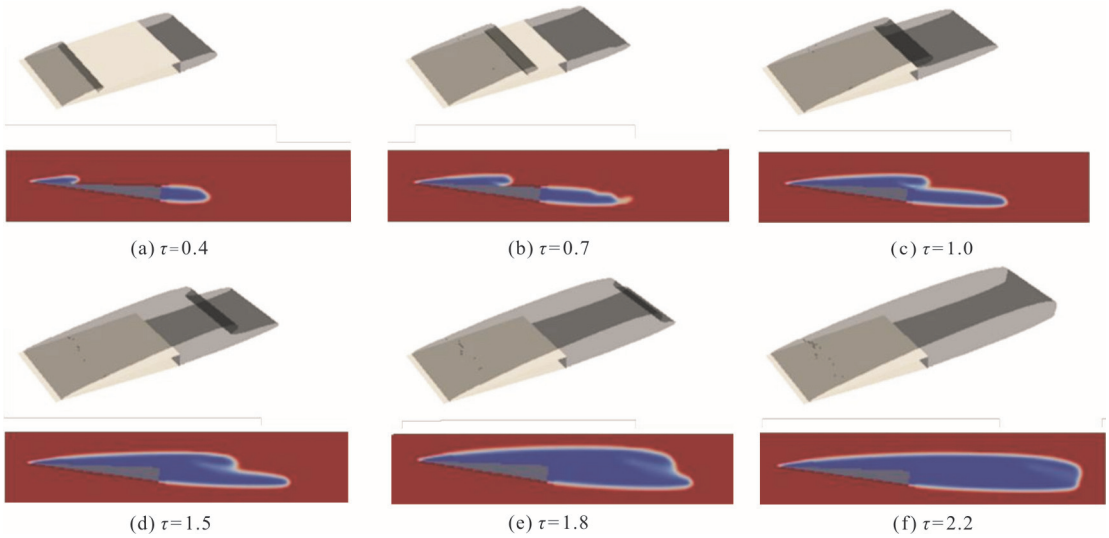

Fig. 9 (Color online) Dimensionless cavity length grow with dimensionless time for the simulated cases at $\mathrm{AOA}=8°$, $\sigma=0.100$ under the free surface effect. The submerged depth over cord length of the hydrofoil $s/c=0.8300$, 1.1625, 1.4950, 1.8275 and 2.1600

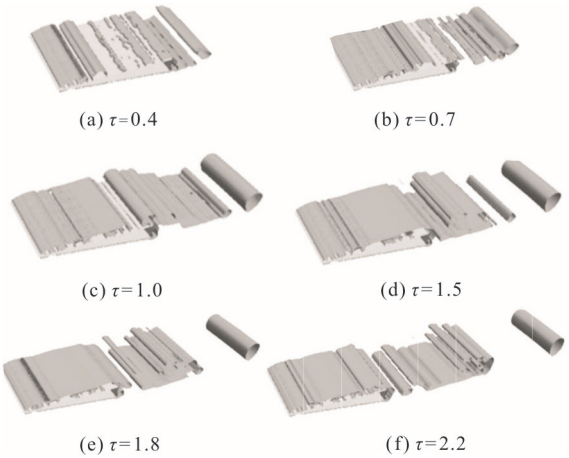

Fig. 10 The added iso-surface of $Q=50\,000$ at $\tau=0.4$ to $\tau=2.2$ for the simulated cases at $\mathrm{AOA}=8°$, $\sigma=0.100$, $s/c=0.8300$ under the free surface effect

the supercavitating flow on the free surface elevation. To examine the interaction between the free surface and supercavitating flow, the time averaged simulated results of the supercavitating flow around the hydrofoil at the submerged depth from $s/c=0.8300$ to 2.1600 are presented in Fig. 11. It shows that the free surface indeed significantly affects the cavity curvature, while the cavity also affects the free surface wave elevation. Both the length and thickness of the cavity over the hydrofoil vary with the submerged depth.

More detailed results are next presented in Figs. 12, 13 regarding the change in the cavity length over chord length (l/c) and maximum cavity thickness over the trailing edge thickness (δ/t) with the depth of submergence, respectively. The cavity over the hydrofoil becomes shorter when the hydrofoil is placed closer to the free surface while the cavity thickness remains almost unchanged. Correspondingly, the effect of the free surface on the cavity shape becomes weaker as the submerged depth increases. It is clear that the influence of the free surface effect on the cavitating flow is found to be around $s/c\le 2.0000$. When s/c is greater than 2, the effect of the free surface on the supercavitating flow around the wedge-shaped hydrofoil is negligible and the case can be essentially considered as a fully submerged problem.

A vertical straight line is added at the trailing edge of the hydrofoil on the midplane in the y-axis direction (see Fig. 1). Figure 14 shows the dimensionless streamwise flow velocity (U/U_∞) distribution along the mentioned line. In order to compare the flow velocity inside the cavity at different submerged depth more clearly, Fig. 15 captures the mentioned dimensionless flow velocity distribution from the upper surface of the hydrofoil towards the edge of the cavity (The fairly sharp change in the velocity gradient indicates the extent of the cavity). The results show that both the flow speed inside and outside the supercavity increase with the submerged depth of the hydrofoil. The flow velocity gradient inside the cavity is greater than the outside. As the submerged depth increases, the higher flow velocity inside the cavity may lead to a smaller cavity curvature and longer cavity length.

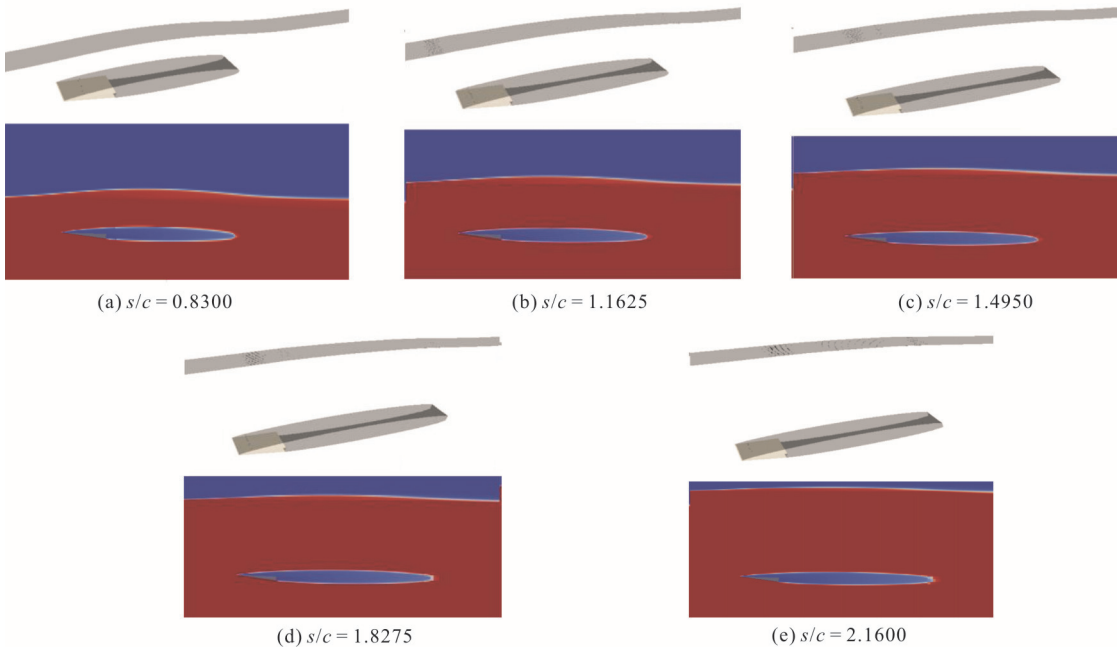

Fig. 11 (Color online) The time averaged results of the supercavitating flow around the hydrofoil at $\mathrm{AOA} = 8°$, $\sigma = 0.100$ under the free surface effect. The cavity shape of the supercavitating flow is shown by the iso-surface at volume fraction of the water equals to 0.5. The submerged depth over cord length of the hydrofoil varies from 0.8300 to 2.1600

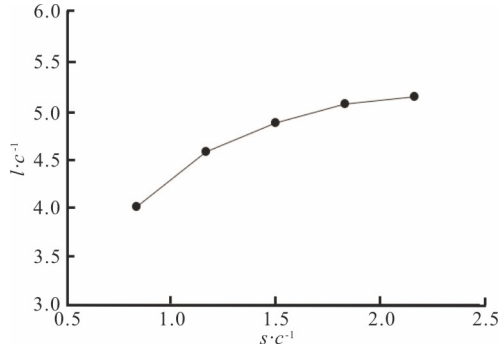

Fig. 12 The simulated results of the cavity length over the chord length of the hydrofoil changes with the various submerged depth under the free surface effect

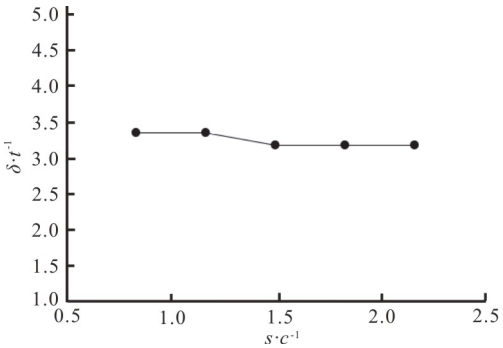

Fig. 13 The simulated results of the maximum cavity thickness over the trail thickness of the hydrofoil changes with the various submerged depth under the free surface effect

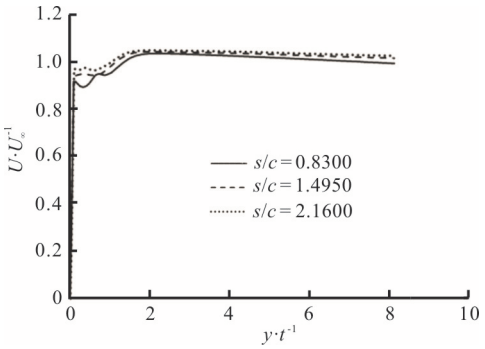

Fig. 14 The dimensionless streamwise flow velocity distribution along the vertical line in the y-axis direction at the trailing edge between the upper surface of the hydrofoil and the free surface at $\mathrm{AOA} = 8°$, $\sigma = 0.100$. The submerged depth over cord length of the hydrofoil varies from 0.8300 to 2.1600. The reference point O can be referred to Fig. 1

Next, the heights of the free surface elevation are examined for various submerged depth of the hydrofoil. Figure 16 shows the dimensionless wave elevation height $((h-s)/c)$ above the supercavitating flow under the free surface effect (Here reference point O is at the trailing edge of the hydrofoil on the midplane shown in Fig. 1). It is worth noting that although the maximum height of the free surface elevation is reduced as the submerged depth increases, the distance between the initially quiescent/

horizontal free surface and hydrofoil (s/c) is still increased. As the hydrofoil moves close to the free surface, the water layer between the upper cavity contour and the free surface become thinner.

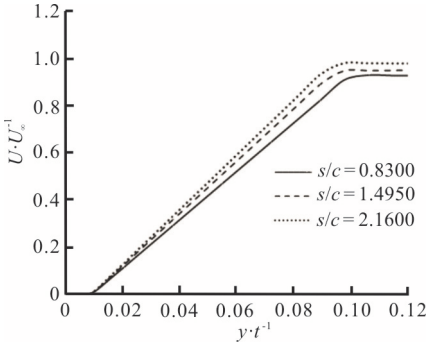

Fig. 15 The dimensionless streamwise flow velocity distribution along the vertical added line in the y-axis direction inside the cavity at $\mathrm{AOA} = 8°$, $\sigma = 0.100$. The submerged depth over cord length of the hydrofoil varies from 0.8300 to 2.1600. The reference point O can be referred to Fig. 1

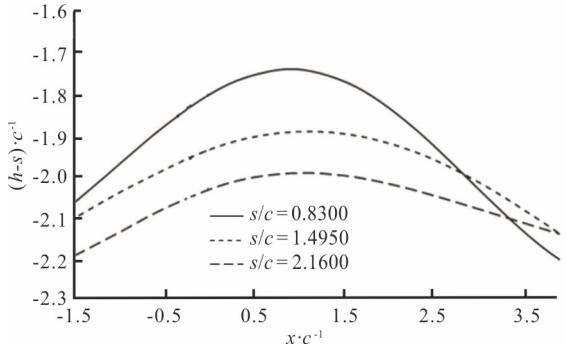

Fig. 16 Effect of the submerged depth on the free surface elevation for the wedge-shaped hydrofoil at $\mathrm{AOA} = 8°$, $\sigma = 0.100$. The submerged depth over cord length of the hydrofoil varies from 0.8300 to 2.1600

2.3 *3-D effect on the supercavitating flow*

Typical simulation cases of the supercavitating flow around the hydrofoil at $\mathrm{AOA} = 8°$, $\sigma = 0.100$, with s/c varies from 0.8300 to 2.1600 are also conducted to analyze the 3-D effects of the supercavitating flow. The simulation uses the same numerical methods and the Cartesian cut-cell mesh with the same characteristics of the grid as described in Section 2.2 for the quasi-3-D cases. Since the aspect ratio (AR) of this hydrofoil is small $(\mathrm{AR} \cong 0.7)$, the 3-D effect on the supercavitating flow is expected, if any, to be strong. Figures 17, 18 present the time averaged simulated results of the cavity profile and the vortex structure of the supercavity at $s/c = 0.8300$ with the full-3-D effects clearly visualized. As the 3-D effect of the hydrofoil start to affect the cavity beginning from the leading edge, the cavitating flow over the hydrofoil becomes much shorter than the equivalent quasi-3-D cases. It indicates that the tip vortices (i.e., streamwise vortices arising from the edge of the hydrofoil) around the hydrofoil can lead to the effective reduction of the angle of attack effect, hence resulting in shorter cavity observed. Besides, both the cavity length and thickness increase as one moves closer to the midspan section of the hydrofoil, where the flow is liken closer to 2-D.

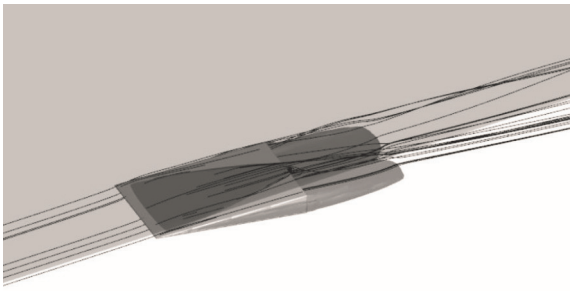

Fig. 17 The time averaged results of the supercavitating flow around the hydrofoil at $\mathrm{AOA} = 8°$, $\sigma = 0.100$, $s/c = 0.8300$ under the 3-D effect. The cavity shape of the supercavitating flow is shown by the iso-surface at volume fraction of the water equals to 0.5. Added are some streamlines around the hydrofoil as shown

Fig. 18 The time averaged simulated results of the vortex structure supercavitating flow around the hydrofoil in full-3-D effect. The added iso-surface of $Q = 50\,000$ at $\mathrm{AOA} = 8°$, $\sigma = 0.100$ and $s/c = 0.8300$

Similar to the results in Section 3.1, the cavity evolution process shown in Fig. 19 with 3-D effects also contains the three stages mentioned earlier: initial strong cavity growth, cavity fusion and stable cavity state. However, since the tip vortices around the hydrofoil affect the length of the cavity, the cavity evolution is also delayed as compared to the quasi-3-D case shown previously in Fig. 9. Figure 20 shows the corresponding vortex structure of the cavitating flow around the hydrofoil during the cavity growth stage based on the Q - criterion[32]. Compared to the quasi-3-D cases, the vortex structure around the hydrofoil is much more complicated, and the tip vortex around the hydrofoil can be clearly seen.

From the qualitative cavitation growth process due to the relatively much shorter span of the hydrofoil studied as compared to the quasi-3-D cases, the 3-D effect on the upper side cavitating flow is

much larger than on the cavitating flow behind the hydrofoil. The upper side cavity length is much shorter than before as for the quasi-3-D cases. Figure 21 depicts quantitatively the cavity length for the quasi-3-D, full-3-D mid-section and 1/4 section with respect to the various submerged depth under the free surface effect. The cavity length under the 3-D effect is reduced by more than 60% on the mid-section and 80% on the 1/4 section compared to the quasi-3-D cases. At the same time, it can be seen that the free surface effect as indicated by the submerged depth on the supercavitating flow in quasi-3-D case is much more significant than the full-3-D case where it is found that the cavity length remains almost unchanged throughout.

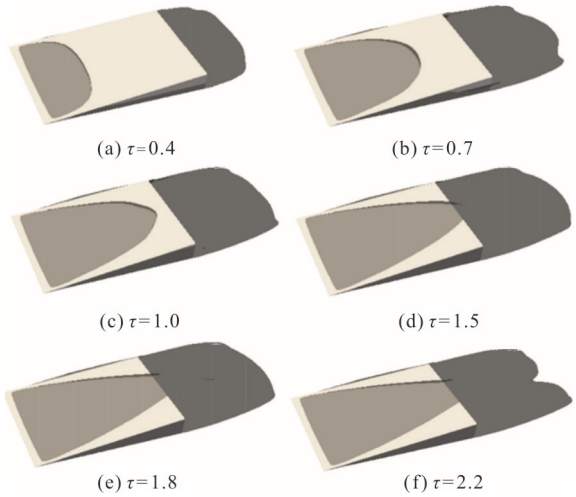

Fig. 19 Cavity evolution from τ =0.4 to $\tau = 2.2$ shown in the simulated results at $\mathrm{AOA} = 8°$, $\sigma = 0.100$ and $s/c = 0.8300$ under the free surface effect

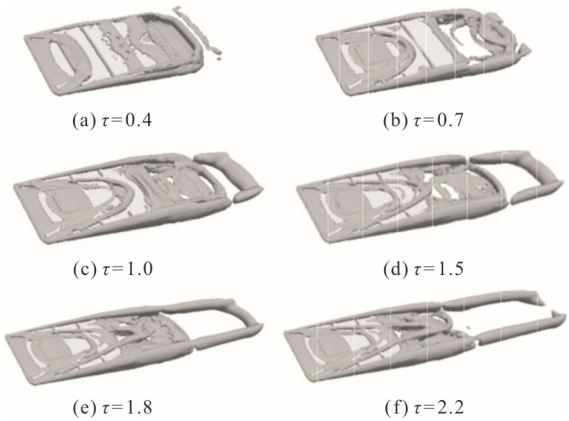

Fig. 20 The added iso-surface of at $\tau = 0.4$ to $\tau = 2.2$ for the simulated cases at $\mathrm{AOA} = 8°$, $\sigma = 0.100$, $s/c = 0.8300$ under the free surface effect

2.4 *Free surface effect on the force coefficients*

The simulated quasi-3-D and full-3-D data at various submerged depths at a constant $\sigma = 0.100$ is studied in this section to analyze the free surface effect on the force coefficients of the wedge-shaped hydrofoil. The submerged depth over cord length of

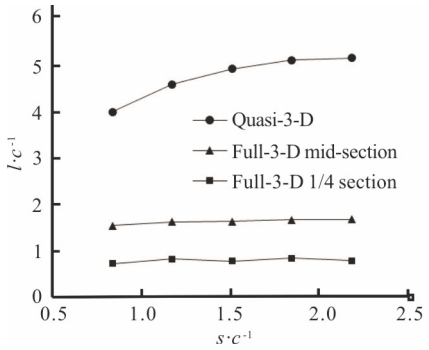

Fig. 21 Comparison of the cavity length for the quasi-3-D versus the full-3-D at mid-section and 1/4 section with respect to the various submerged depth under the free surface effect

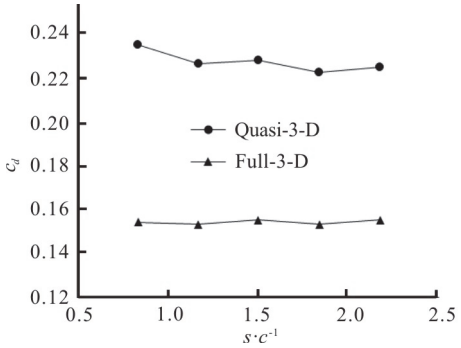

Fig. 22 The simulated results of the lift coefficient for the supercavitating hydrofoil at $\mathrm{AOA} = 8°$, $\sigma = 0.100$ under the free surface effect. The submerged depth over cord length of the hydrofoil varies from 0.8300 to 2.1600

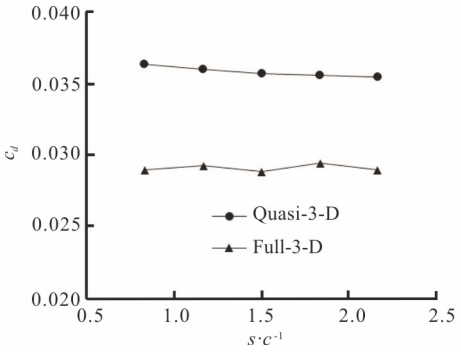

Fig. 23 The simulated results of the drag coefficient for the supercavitating hydrofoil at $\mathrm{AOA} = 8°$, $\sigma = 0.100$ under the free surface effect. The submerged depth over cord length of the hydrofoil varies from 0.8300 to 2.1600

the hydrofoil varies from 0.8300 to 2.1600 at the given $AOA = 8°$. The results in Figure 22 shows the quasi-3-D results first. The lift coefficient (c_l) decreases as the submerged depth increases in a rather monotonic manner and tending towards a constant under the gravity effect and wave effect. Very possibly, the interplay between the gravity and the surface wave contributes towards such a behavior of the couplings effect. As also similarly seen in Section 3.2, the effect of free surface diminishes as s/c approaches 2.0000. Figure 23 shows that the drag coefficient (c_d) decreases marginally as the submerged depth increases. The force coefficients only vary in a small range.

For the full-3-D cases, since the curvature of the supercavitating flow over the hydrofoil (cavity length and cavity thickness) is significantly reduced under the 3-D effect, the nearby free surface has minor effect on the supercavitating flow. The lift and drag coefficient of the full-3-D cases are basically unchanged at s/c varies from 0.8300 to 2.1600: in particular c_l is about 0.154, c_d is about 0.029 as shown in the respective figures.

3. Conclusions

In this study, the supercavitating flow around a wedge-shaped hydrofoil under the free surface effect is analyzed by CFD with Cartesian cut-cell mesh method, in which the VOF method, the k-ε turbulence model with the Schnerr Sauer cavitation model is applied to calculate the supercavitating turbulent flow. The simulated quasi-3-D results are compared to the experimental data by Dawson[29], the analytical solution of Faltinsen and Semenov[7] and Wu's theory[31] at three angles of attack (8°, 10°, 12°) when the submerged depth over cord length of the hydrofoil is set equal to 0.8300. The results are consistent with each other, which validate the accuracy of the numerical methods.

Cavity evolution process of the quasi-3-D flow is analyzed first, which include three stages: initial cavity growth, cavity fusion and stable cavity state. In the cavity growth stage, the cavitating flow is generated both on the upper side and back of the hydrofoil and grows backwards over time. In the second stage, the cavities fuse at $\tau \cong 1.5$, and after fusion, the cavitating flow continue to grow backwards to the final stable state. The growth of the cavitating flow generally stopped after then. Typical full-3-D cases for the low aspect ratio hydrofoil are also conducted to analyze the 3-D effects. The tip vortices around the hydrofoil have induced and led to a much shorter cavity than the quasi-3-D cases.

The simulation of the supercavitating flow around the hydrofoil is carried out at various submerged depths to analyze the free surface effect on the cavity profile and force coefficients. The results show that the free surface will strongly affect the cavity curvature, while at the same time, the cavity also affects the wave elevation. Cavity will become shorter and thicker when moving closer to the free surface, while the growth rate of the cavity decreases with the submerged depth of the hydrofoil under the free surface effect. In our study, it is found that the presence of the free surface effect and its effect on the cavity length becomes negligible as $s/c \geq 2.0000$. Results of the full-3-D cases are also analyzed and compared with the quasi-3-D cases. The cavity length of the supercavitating flow under the 3-D effect is reduced by more than 60% due to the tip vortices around the hydrofoil. As the free surface mostly affects the cavitating flow on the upper side of the hydrofoil, the free surface effect in the quasi-3-D cases is much more significant than the full-3-D cases.

Generally, the quasi-3-D numerical results show that the force coefficients decrease as the submerged depth increases and the force coefficients only vary in a small range. Slight oscillations are observed in the results under the coupling effects of the gravity and wave near the supercavitating flow. For the full-3-D cases, the force coefficients are basically unchanged. The results of this study present the free surface effect on high-speed cruising for the wedge-shaped hydrofoil. It is surmised that for other hydrofoil shape say with camber or even geometrical variation in the spanwise direction, the findings would be moderated but the numerical approach employed as in this work should still apply.

References

[1] Franc J. P., Michel J. M. Fundamentals of cavitation [M]. Berlin, Germany: Springer science and Business media, 2006.

[2] Wang G., Senocak I., Shyy W. et al. Dynamics of attached turbulent cavitating flows [J]. *Progress in Aerospace Sciences*, 2001, 37(6): 551-581.

[3] Wang Y., Wu X., Huang C. et al. Unsteady characteristics of cloud cavitating flow near the free surface around an axisymmetric projectile [J]. *International Journal of Multiphase Flow*, 2016, 85: 48-56.

[4] Xu C., Huang J., Wang Y. et al. Supercavitating flow around high-speed underwater projectile near free surface induced by air entrainment [J]. *AIP Advances*, 2018, 8(3): 035016.

[5] Xu C., Wang Y. W., Huang C. G. et al. The effect of free surface on cloud cavitating flow around a blunt body [J]. *Journal of Hydrodynamics*, 2017, 29(6): 979-986.

[6] Xu C., Wang Y., Huang C. et al. Cloud cavitating flow that surrounds a vertical hydrofoil near the free surface [J]. *Journal of Fluids Engineering*, 2017, 139(10): 101302.

[7] Faltinsen O. M., Semenov Y. A. The effect of gravity and

cavitation on a hydrofoil near the free surface [J]. *Journal of Fluid Mechanics*, 2008, 597: 371-394.

[8] Franc J. P., Michel J. M. Attached cavitation and the boundary layer: Experimental investigation and numerical treatment [J]. *Journal of Fluid Mechanics*, 1985, 154: 63-90.

[9] Kuiper G. Cavitation research and ship propeller design [J]. *Applied Scientific Research*, 1997, 58(1-4): 33-50.

[10] Hrubes J. High-speed imaging of supercavitating underwater projectiles [J]. *Experiments in Fluids*, 2001, 30(1): 57-64.

[11] Leroux J. B., Coutier-Delgosha O., Astolfi J. A. A joint experimental and numerical study of mechanisms associated to instability of partial cavitation on two-dimensional hydrofoil [J]. *Physics of Fluids*, 2005, 17(5): 052101.

[12] Wei Y. P., Wang Y., Fang X. et al. A scaled underwater launch system accomplished by stress wave propagation technique [J]. *Chinese Physics Letters*, 2011, 28(2): 024601.

[13] Dular M., Bachert B., Stoffel B. et al. Relationship between cavitation structures and cavitation damage [J]. *Wear*, 2004, 257(11): 1176-1184,.

[14] Dular M., Bachert R., Stoffel B. et al. Experimental evaluation of numerical simulation of cavitating flow around hydrofoil [J]. *European Journal of Mechanics-B/Fluids*, 2005, 24(4): 522-538.

[15] Heindel T. J. A review of X-ray flow visualization with applications to multiphase flows [J]. *Journal of Fluids Engineering*, 2011, 133(7): 074001.

[16] Coutier-Delgosha O., Deniset F., Astolfi J. A. et al. Numerical prediction of cavitating flow on a two-dimensional symmetrical hydrofoil and comparison to experiments [J]. *Journal of Fluids Engineering*, 2007, 129(3): 279-292.

[17] Coutier-Delgosha O., Reboud J. L., Delannoy Y. Numerical simulation of the unsteady behaviour of cavitating flows [J]. *International Journal for Numerical Methods in Fluids*, 2003, 42(5): 527-548.

[18] Zhou L., Wang Z. Numerical simulation of cavitation around a hydrofoil and evaluation of a RNG $k-\varepsilon$ model [J]. *Journal of Fluids Engineering*, 2008, 130(1): 011302.

[19] Wu J. Y., Wang G. Y., Shyy W. Time-dependent turbulent cavitating flow computations with interfacial transport and filter-based models [J]. *International Journal for Numerical Methods in Fluids*, 2005, 49(7): 739-761.

[20] Huang B., Zhao Y., Wang G. Large eddy simulation of turbulent vortex-cavitation interactions in transient sheet/cloud cavitating flows [J]. *Computers and Fluids*, 2014, 92: 113-124.

[21] Ji B., Luo X., Arndt R. E. A. et al. Numerical simulation of three dimensional cavitation shedding dynamics with special emphasis on cavitation-vortex interaction [J]. *Ocean Engineering*, 2014, 87: 64-77.

[22] Merkle C. L., Deutsch S. Microbubble drag reduction in liquid turbulent boundary layers [J]. *Applied Mechanics Reviews*, 1992, 45(3): 103-127.

[23] Elbing B. R., Mäkiharju S., Wiggins A. et al. On the scaling of air layer drag reduction [J]. *Journal of Fluid Mechanics*, 2013, 717: 484-513.

[24] Elbing B. R., Winkel E. S., Lay K. A. et al. Dowling, and M. Perlin. Bubble-induced skin-friction drag reduction and the abrupt transition to air-layer drag reduction [J]. *Journal of Fluid Mechanics*, 2008, 612: 201-236.

[25] Yu X., Wang Y., Huang C. et al. Experiment and simulation on air layer drag reduction of high-speed underwater axisymmetric projectile [J]. *European Journal of Mechanics-B/Fluids*, 2015, 52: 45-54.

[26] Ceccio S. L. Friction drag reduction of external flows with bubble and gas injection [J]. *Annual Review of Fluid Mechanics*, 2010, 42: 183-203.

[27] Zou W., Yu K., Arndt R. E. A. et al. On the shedding of the ventilated supercavity with velocity disturbance [J]. *Ocean Engineering*, 2013, 57: 223-229.

[28] Wang Z., Huang B., Wang G. et al. Experimental and numerical investigation of ventilated cavitating flow with special emphasis on gas leakage behavior and re-entrant jet dynamics [J]. *Ocean Engineering*, 2015, 108: 191-201.

[29] Dawson T. E. An experimental investigation of a fully cavitating two-dimensional flat plate hydrofoil near a free surface [D]. Doctoral Thesis, Pasadena, USA: California Institute of Technology, 1962.

[30] Yuan W., Sauer J., Schnerr G. H. Modeling and computation of unsteady cavitation flows in injection nozzles [J]. *Mécanique and Industries*, 2001, 2(5): 383-394.

[31] Wu T. Y. T. A wake model for free-streamline flow theory Part 1. Fully and partially developed wake flows past an oblique flat plate [J]. *Journal of Fluid Mechanics*, 1962, 13: 161-181.

[32] Hunt J. C., Wray A. A., Moin P. Eddies, streams, and convergence zones in turbulent flows [R]. Center for Turbulence Research Report CTR-S88, 1988, 193.